Electronic structure and magnetism in *P*4/*nmm* KCoO₂

Ozan Dernek [,1] Santosh Kumar Radha,[2] Jerome Jackson [,3] and Walter R. L. Lambrecht [1]

[1]*Department of Physics, Case Western Reserve University, 10900 Euclid Avenue, Cleveland, Ohio 44106-7079, USA*
[2]*Agnostiq Inc., 325 Front St W, Toronto, Ontario, Canada M5V 2Y1*
[3]*Scientific Computing Department, STFC Daresbury Laboratory, Warrington WA4 4AD, United Kingdom*

KCoO₂ has been found in 1975 to exist in a unique structure with $P4/nmm$ space group featuring Co atoms in a square pyramidal coordination. The Co atoms in the plane are linked by O in a square arrangement reminiscent of the cuprates. However, its electronic structure has not been studied until now. Unlike Co atoms in LiCoO₂ and NaCoO₂, which are in octahedral coordination and are nonmagnetic band structure insulators, the unusual coordination of d^6 Co³⁺ in KCoO₂ is here shown to lead to a magnetic stabilization of an insulating structure with high magnetic moments of $4\mu_B$ per Co. The electronic band structure is calculated using the quasiparticle self-consistent (QS)GW method and the basic formation of magnetic moments is explained in terms of the orbital decomposition of the bands. The optical dielectric function is calculated using the Bethe-Salpeter equation including only transitions between equal spin bands. The magnetic moments are shown to prefer an antiferromagnetic ordering along the [110] direction. Exchange interactions are calculated from the transverse spin susceptibility and a rigid spin approximation. The Néel temperature is estimated using the mean-field and Tyablikov methods and found to be between ∼100 and ∼250 K. The band structure in the AFM ordering can be related to the FM ordering by band folding effects. The optical spectra are similar in both structures and show evidence of excitonic features below the quasiparticle gap of ∼4 eV.

I. INTRODUCTION

Among the alkali oxocobaltates, LiCoO₂ and NaCoO₂ have received much more attention than the larger cation ones because of their role in Li-ion batteries and the reported superconductivity in hydrated Na₁/₃CoO₂:H₂Oᵧ. Both of these exhibit the layered $R\bar{3}m$ structure, which can be viewed as consisting of edge sharing, octahedrally coordinated CoO₂ layers with a triangular Co lattice stacked in an ABC stacking with intercalated Li or Na. The octahedral coordination, splitting d levels in a sixfold degenerate t_{2g}, and a fourfold degenerate e_g level, leads to a simple nonmagnetic insulating band structure for the d^6 configuration of Co³⁺ resulting from Li or Na donating their electron to the CoO₂ planes. However, starting with K, the alkali ions are too large to fit in this structure. Only half the amount of K can be maintained in between CoO₂ layer in this KₓCoO₂ structure. For larger x, this structure becomes unstable and other structures were reported. In 1975, two different synthesis methods for KCoO₂ were reported and led to two totally different crystal structures with different Co coordination. The first is a unique layered structure with square pyramidal coordination, with the $P4/nmm$ space group [1]. The other is a stuffed cristobalite-type structure in which Co is tetrahedrally coordinated with O in an open network of corner sharing tetrahedra, filled with K ions. Two related forms with space groups $I\bar{4}$ and $I\bar{4}2d$ were found and called respectively β and α-KCoO₂ [2]. Besides these two papers, there seem to be no other experimental studies reported on KCoO₂. Only very recently, a new synthesis method was developed for KCoO₂ in the pyramidal coordination and $P4/nmm$ space group [3]. KCoO₂ in the $P4/nmm$ structure was recently identified as a candidate for K batteries in a computational theoretical search based on structures available in Materials Project [4]. It was found to have a rather high diffusion barrier for K compared to Li and Na in their corresponding cobaltates, which makes it less attractive as cathode material although it was found to have a high theoretical capacity. Besides a magnetic moment of $2.99 \mu_B$, no details on its electronic structure of magnetic properties were provided in this study.

Because of the occurrence of a square coordination of CoO₂, which resembles that of CuO₂ in high-T_c materials, this phase may be of interest for nonconventional superconductivity. We will further show that it is actually antiferromagnetic and in that sense may play the role of the La₂CuO₄ parent compound of high-T_c superconductors. The occurrence of a d^6 in other than the octahedral environment is of interest because it has particular stability in the octahedral environment where it exactly fills the lower t_{2g} levels and leads to a simple band insulating behavior. In the pyramidal or tetrahedral environment this is not the case, hence we expect that stabilization of these environments requires formation of a magnetic moment. The square pyramidal environment in the $P4/nmm$ structure is highly unusual such that a closely bound O and an electropositive K ion occur on the opposite sides of the square plane. Here we present first-principles electronic structure calculations of this material, which lead to a basic understanding of its magnetic properties.

II. COMPUTATIONAL METHODS

The calculations in this study combine density functional theory (DFT) with many-body perturbation theory (MBPT).

While DFT is used as a starting point for the electronic structure, the generalized gradient approximation (GGA) (used here in the Perdew-Burke-Ernzerhof (PBE) parametrization [5]) is not sufficiently accurate to make accurate predictions for band gaps and optical properties. To calculate the quasiparticle band structure, we use Hedin's GW method [6,7] in which G is the one-electron Green's function and W is the screened Coulomb interaction. More specifically, we here use the quasiparticle self-consistent version of GW ($QSGW$) [8,9], which becomes independent of the starting DFT approximation by including a nonlocal exchange correlation potential extracted from the GW self-energy and updating the noninteracting H_0 Hamiltonian. By noninteracting, we here mean that the dynamical (energy-dependent) interactions are not included but only a static interaction as in DFT.

The band structure method used to solve the Kohn-Sham equations underlying both the DFT and $QSGW$ method is the full-potential linearized muffin-tin orbital (FP-LMTO) method as implemented in the QUESTAAL codes [10]. This is an augmentation method in which the basis set consists of atom-centered smoothed Hankel function spherical waves [11], *augmented* inside the muffin-tin spheres with solutions of the radial Schrödinger equation of the all-electron potential at a linearization energy and their energy derivatives. Core states, calculated with atomic boundary conditions at the muffin-tin radius, are thus fully included in the charge density (thereby including core-valence exchange) and semicore states are further included in the basis set as *local orbitals* with a fixed boundary condition at the sphere radii. Here we include K $3p$ states as local orbitals.

In the LMTO implementation of the GW method, two-point quantities such as the bare and screened Coulomb interaction are expanded in an auxiliary mixed product basis set, which incudes products of partial waves inside the spheres and interstitial plane waves. Such a basis set is more efficient than a plane-wave basis set to describe the screening and reduces the need to include high-energy empty bands.

The optical dielectric function is calculated using the Bethe-Salpeter equation (BSE) in the Tamm-Dancoff approximation and using a static W [12] as implemented by Cunningham *et al.* [13] in the LMTO basis set within the QUESTAAL package.

The basis set and other convergence parameters are discussed along with the results. A well-converged Γ-point centered **k** mesh of $8 \times 8 \times 4$ and the tetrahedron method are used for the Brillouin zone integrations in the DFT calculations. The atom-centered basis set allows us to interpolate the GW self-energy via a Fourier transform to real space and back to any desired **k** point even when using a somewhat coarser $5 \times 5 \times 3$ mesh of points on which the GW self-energy is evaluated. The BSE calculations are performed including 24 valence and 16 conduction bands per primitive cell.

To study the magnetic exchange interactions, we use the approach of Kotani and van Schilfgaarde [14], which extracts the exchange interactions from the transverse spin susceptibility within a rigid spin approximation within each muffin-tin sphere. The noninteracting spin-spin response function is first calculated from the spin-dependent $QSGW$ eigenstates and

eigenvalues,

$$
\chi_{\mathbf{q}}^{0+-}(\mathbf{r}, \mathbf{r}', \omega)
$$

$$
= \sum_{\mathbf{k}n\downarrow}^{occ} \sum_{\mathbf{k}'n'\uparrow}^{unocc} \frac{\Psi_{\mathbf{k}n\downarrow}^*(\mathbf{r})\Psi_{\mathbf{k}'n'\uparrow}(\mathbf{r})\Psi_{\mathbf{k}'n'\uparrow}^*(\mathbf{r}')\Psi_{\mathbf{k}n\downarrow}(\mathbf{r}')}{\omega - (\epsilon_{\mathbf{k}'n'\uparrow} - \epsilon_{\mathbf{k}n\downarrow}) + i\delta}
$$

$$
+ \sum_{\mathbf{k}n\downarrow}^{unocc} \sum_{\mathbf{k}'n'\uparrow}^{occ} \frac{\Psi_{\mathbf{k}n\downarrow}^*(\mathbf{r})\Psi_{\mathbf{k}'n'\uparrow}(\mathbf{r})\Psi_{\mathbf{k}'n'\uparrow}^*(\mathbf{r}')\Psi_{\mathbf{k}n\downarrow}(\mathbf{r}')}{-\omega - (\epsilon_{\mathbf{k}n\downarrow} - \epsilon_{\mathbf{k}'n'\uparrow}) + i\delta}, \quad (1)
$$

with $\mathbf{k}' = \mathbf{k} + \mathbf{q}$. It is then coarse grained by averaging over the spheres, which constitutes the rigid spin approximation,

$$
D^0(\mathbf{q}, \omega)_{aa'} = \int_a d^3r \int_{a'} d^3r' \bar{e}_a(\mathbf{r}) \chi_{\mathbf{q}}^{0+-}(\mathbf{r}, \mathbf{r}', \omega) \bar{e}_{a'}(\mathbf{r}'), \quad (2)
$$

with $e_a(\mathbf{r}) = M_a(\mathbf{r})/M_a$, $M_a = \int_a d^3r M_a(\mathbf{r})$, $\bar{e}_a = e_a(\mathbf{r})/\int_a d^3r |e_a(\mathbf{r})|^2$. So the $\bar{e}_a(\mathbf{r}) \propto e_a(\mathbf{r})$ is a vector along the local magnetization density $M_a(\mathbf{r}) = n_\uparrow(\mathbf{r}) - n_\downarrow(\mathbf{r})$, normalized by the total moment per sphere M_a, which is normalized by $\int_a d^3r \bar{e}_a(\mathbf{r}) e_a(\mathbf{r}) = 1$. Following Antropov [15], the exchange interactions defined by

$$
J_{\alpha\beta}(\mathbf{r}, \mathbf{r}') = -\frac{\delta^2 E}{\delta M_\alpha(\mathbf{r})\delta M_\beta(\mathbf{r}')} \quad (3)
$$

corresponds to the inverse of the transverse susceptibility $J = \chi^{-1}$ because the changes in magnetization originate from an external magnetic field and χ is the response function vs the external magnetic field. This differs from the above noninteracting susceptibility, which defines the response with respect to the total field, including the one generated by the interactions. Assuming now that the similarly sphere-averaged interaction term is **q** independent and site diagonal, $\bar{U}_{aa'}(\mathbf{q}, \omega) = \bar{U}_a(\omega)\delta_{aa'}$ Kotani and van Schilfgaarde show that one can find $\bar{U}_a(\omega)$ by requiring to fulfill a sum rule and the $\omega \to \infty$ asymptotic behavior. This then yields directly the inverse of the interacting $D(\mathbf{q}, \omega)$ as

$$
[D(\mathbf{q}, \omega)]_{aa'}^{-1} = \frac{\omega}{M_a}\delta_{aa'} - \bar{J}_{aa'}(\mathbf{q}, \omega),
$$

$$
\bar{J}_{aa'}(\mathbf{q}, \omega) = -[D^0(\mathbf{q}, \omega)]_{aa'}^{-1}
$$

$$
+ \left(\sum_b M_b [D^0(\mathbf{q} = 0, \omega)]_{ba}^{-1}/M_a \right)\delta_{aa'}. \quad (4)
$$

This $\bar{J}_{aa'}$ is closely related to the Heisenberg exchange interactions, as discussed further in [14],

$$
[D^{\mathcal{H}}(\mathbf{q}, \omega)]_{aa'}^{-1} = \frac{\omega}{M_a}\delta_{aa'} - J^{\mathcal{H}}(\mathbf{q}), \quad (5)
$$

which suggest taking $J^{\mathcal{H}}(\mathbf{q}) = J(\mathbf{q}, \omega = 0)_{aa'}$, i.e., the static limit. Here $J_{aa'}$ differs from $\bar{J}_{aa'}$ only by removing the on-site term of $[D^0]^{-1}$. Although, we sketched here the more general presentation of [14] of the enhanced susceptibility, in the end, we obtain the exchange interactions from the static version of the inverse of the bare susceptibility $[D^0]^{-1}$. This is also compatible with the Liechtenstein *et al.* multiple scattering formulation of the linear response theory [16].

The Heisenberg exchange interactions in real space $J_{a,a'}^{0\mathbf{T}}$ can then be obtained by inverting the Bloch sum $J_{aa'}(\mathbf{q}) = \sum_{\mathbf{T}} e^{i\mathbf{q}\cdot\mathbf{T}} J_{a,a'}^{0\mathbf{T}}$, i.e., by an integral over the Brillouin zone.
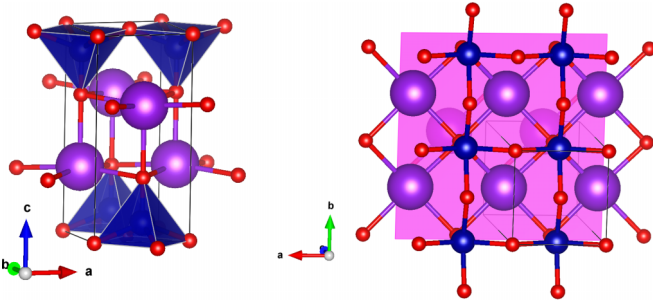
FIG. 1. $P4/nmm$ crystal structure of $KCoO_2$ in two different projections, the first emphasizing the square pyramidal coordination of Co, and the second projecting on the c plane emphasizing the Co-O square arrangement reminiscent of the cuprates. Small red spheres are O, large blue spheres in the center of the pyramids are Co, and the pink large spheres are K.

Thus, if we calculate the $J_{aa'}(\mathbf{q})$ on a $N \times N \times N$ mesh in the Brillouin zone, then a discrete inverse Fourier transform gives us the $J_{a,a}^{0\mathbf{T}}$ in a $N \times N \times N$ supercell, or the exchange interactions out to a distance $|\boldsymbol{\tau}_{a'} - \boldsymbol{\tau}_a + \mathbf{T}_{max}|$ where $\boldsymbol{\tau}_a$ is the position in the unit cell of the atom labeled a. $\mathbf{T}_{max}$ is the largest lattice translation vector corresponding to the superlattice.

We can then use various methods to estimate the critical temperature T_c, such as the mean-field approximation, or the random phase approximation (RPA) developed by Tyablikov *et al.* [17] and Callen [18] and more recently used by Rusz *et al.* [19]. In the case (which occurs here) of several magnetic sites per unit cell, the critical temperature in the mean-field approximation is obtained by diagonalizing the matrix of the $J_{ab}^0 = \sum_{\mathbf{T}} J_{ab}^{0\mathbf{T}}$, where if $a = b$, the on-site term J_{aa}^{00} is excluded from the sum,

$$\sum_b \left[J_{ab}^0 - j\delta_{ab} \right] \langle S_b \rangle = 0. \tag{6}$$

The mean-field critical temperature is then given by $k_B T_c = 2 j_{max}/3$ with j_{max} the highest eigenvalue [20]. The normalized eigenvectors tell us the relation of the average spins on the sites in the cell, i.e., the type of magnetic ordering. The mean-field critical temperature is used as starting point for the RPA iterative procedure. Typically, the latter gives an underestimate while the mean-field method gives an upper limit.

III. RESULTS

A. Band structure and magnetic moments in ferromagnetic structure

The crystal structure is shown in Fig. 1. In our calculations, we used the structural information [21] obtained by the Materials Project [22] in the generalized gradient approximation (GGA), listed as data set mp-20528. The tetragonal lattice constants are $a = 3.8482$, $c = 8.0021$ Å. These are about 1% larger that the experimental values given in the Inorganic Crystalline Structure Database (ICSD) ICSD-15770 referring to the original data of Ref. [1]. The Wyckoff positions of the atoms in the primitive unit cell and the .cif (crystallographic information files) can be found there.

There are two types of O, the $O_{(1)}$ lying close to the K **c** plane, which are strongly bonded to the Co in the z direction at a bond distance of 1.741 Å, and the $O_{(2)}$, which lie in the Co-$O_{(2)}$ layer and have a bond length to Co of 2.063 Å. The K-$O_{(1)}$ in-**c**-plane bond length is 2.732 Å and along the **c** axis is 2.791 Å. Within spin-polarized GGA, we find a high magnetic moment of $4\,\mu_B$ per Co atom and a ferromagnetic semiconductor band structure with a small gap.

The high magnetic moment can be understood as follows. In a pyramidal environment, the local point group is C_{4v}. The point group of the crystal is D_4 because the two formula units per cell are related by an inversion center. The d states will split into a_1 ($3z^2 - r^2$), b_1 ($x^2 - y^2$), b_2 (xy), and orbitally doubly degenerate e (xz, yz) states, as labeled by their irreducible representations. The spin polarization is clearly induced by putting two electrons with parallel spin in the doubly degenerate state, which is favored by Hund's rule. This then induces spin splittings in the other states. From the detailed orbital analysis of the bands given later, we can see that for the xz, yz like states, the spin splitting between majority and minority spin is larger than 10 eV. Apparently, the induced splitting in the $3z^2 - r^2$ and $x^2 - y^2$ states is similar and keeps their minority spin states empty but the spin splitting of the xy state is smaller and keeps both majority and minority bands derived from the xy orbitals filled. Hence, the configuration can be described as $b_{2\uparrow}^2 e_{\uparrow}^2 a_{1\uparrow}^1 b_{1\uparrow}^1$ and results in a net magnetic moment of $4\mu_B$. The reason why the xy states have a smaller spin splitting is less obvious at this point but will be addressed later by examining the band orbital composition.

The spin splitting is the larger energy scale compared to crystal field splittings. In an octahedral environment, e_g states ($x^2 - y^2$, $3z^2 - r^2$) are well known to lie above the t_{2g} states (xy, xz, yz) because the former points most directly to surrounding anion charges. In a square pyramidal environment there is only one apical O in the z direction ($O_{(1)}$) and in the present case there is an opposite charge of K on the other side. Even though the bond length of $O_{(1)}$ to Co in the z direction is smaller than the bond lengths to $O_{(2)}$ in the plane, this will lower the $3z^2 - r^2$ relative to the $x^2 - y^2$ and the xz, yz relative to xy. The band analysis below will show that for the same spin, the typical splitting between $x^2 - y^2$ and $3z^2 - r^2$ or between xz, yz and xy is in order of 1–2 eV, significantly smaller than the spin splitting.

One can also view this from the perspective of forming bonding and antibonding states with O-p orbitals. The $3z^2 - r^2$ and $x^2 - y^2$ point directly to O-p orbitals, forming strong σ-type bonding and antibonding states while the xz, yz, xy states can only form weaker π bonds. The xy states form π bonding and antibonding states with four O-p states in the plane, while the xz state form π bonds with only three oxygens. However, the ordering of the corresponding bands depends on whether these bands have bonding or antibonding character. There is in fact strong hybridization between O-p and Co-d. The high spin splitting results in the majority spin states of Co-d_e states being pushed below the O-2p so that the bonding states have more Co character and the antibonding states have more O character. Therefore, we find a rather strong majority spin O-p character near the top of the valence band. On the other hand, for the minority spin states, the opposite is true. They lie above the O-2p, hence the antibonding
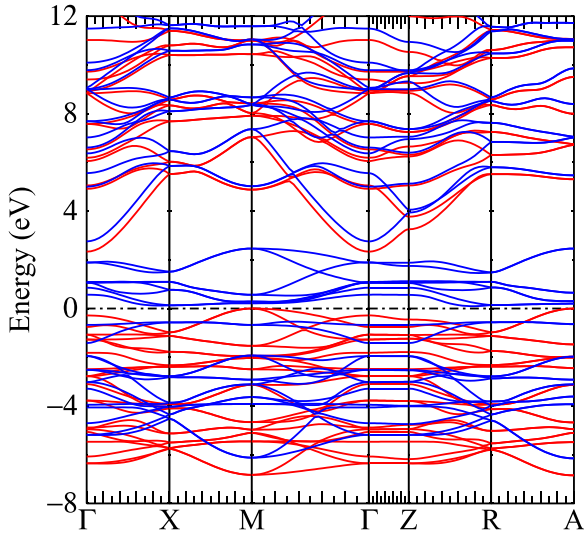
FIG. 2. Spin-polarized band structure in GGA of $KCoO_2$ in the $P4/nmm$ phase, red majority spin, blue minority spin.

TABLE I. Band gaps in $P4/nmm$ $KCoO_2$ in QSGW approximation.

Type	k_v	k_c	Spin type	Gap (eV)
direct	M	M	↑↓	3.99
indirect	M	Γ	↑↑	5.07
direct	M	M	↑↑	8.38
direct	Γ	Γ	↑↑	5.90
indirect	0.8Z-R	M	↓↓	4.83
direct	M	M	↓↓	4.95
direct	0.8Z-R	0.8Z-R	↓↓	5.05

states are Co-like. There remains the question why the xy states have a smaller spin splitting. The two Co atoms in the unit cell lie slightly above and below the O plane along a [110] direction, thus their xy orbitals point directly to each other. This would indicate stronger Co-Co band formation, hence delocalizes these states, which could qualitatively explain the lower spin polarization since these spins become more itinerant.

The spin-polarized band structure at the GGA level is shown in Fig. 2. Interestingly, a small gap opens between spin-up and spin-down bands with rather flat bands. The GGA result is sensitive to details of the calculation. For example, in Materials Project (mp-20258), the gap is listed as zero, although a integer magnetic moment of $4\mu_B$, characteristic of an insulator, is obtained. The gap becomes significantly larger in the QSGW method as seen in Fig. 3. We can see that the
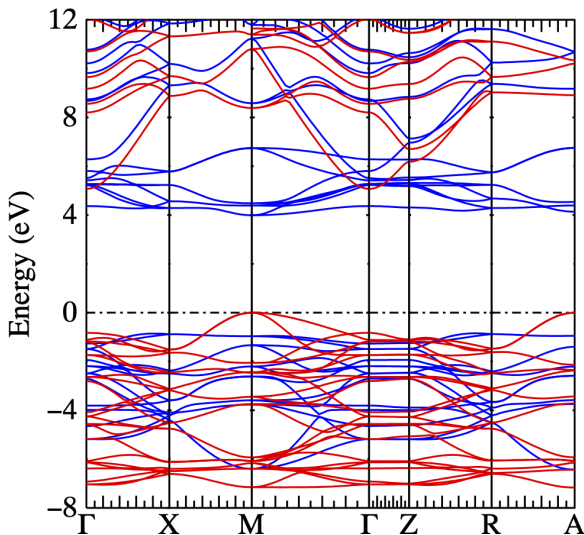

FIG. 3. Band structure of $KCoO_2$ in QSGW approximation for the $P4/nmm$ structure. Red majority spin, blue minority spin.

valence band maximum (VBM) occurs at M for the majority spin while the conduction band minimum (CBM) has minority spin character. The reason why the VBM occurs at M is that the antibonding interaction of the $x^2 - y^2$ orbitals with O-$p\sigma$ orbitals is optimized at this **k** point by the Bloch function phase factors because the same sign lobes point toward the Co for each O along in the square coordination of Co. The majority spin CBM occurs at Γ. The majority spin highest valence band is quite flat. The majority spin and minority spin band gaps are staggered with respect to each other. The relevant gaps are summarized in Table I. These calculations used a 2κ LMTO basis set with smoothed Hankel function envelope functions up to $l = 2$ ($spdspd$) for K and O, and ($spdfspd$) for Co. Without the Co-f, the gap is slightly higher (4.17 eV).

The total and partial densities of states (PDOS) on various orbitals are shown in Fig. 4. The orbital contributions of the bands are shown in Figs. 5–7. The PDOS refers to a partial wave decomposition while the bands correspond to a decomposition in muffin-tin-orbital basis functions. These results were obtained with the slightly smaller basis set without the Co-f basis functions but for the qualitative features, this is of no importance. The PDOS and colored band plots provide consistent information.

We can see that the bands with predominantly xy character are filled for both spins. On the other hand, the minority spin $x^2 - y^2$, $3z^2 - r^2$, and xz, yz contributions occur mostly in the empty bands. This is consistent with the above described origin of the large magnetic moment of $4\mu_B$. The valence bands also have a significant contribution from O-p as shown in Fig. 6. The K contributions (shown in Fig. 7), as expected, occur mostly in the conduction band. They do not contribute significantly to the lower lying set of minority spin bands. This is consistent with K donating electron to the CoO_2 layer.

One can further see that the majority spin VBM in terms of Co-d has mostly $x^2 - y^2$ contribution but its dominant character is $O_{(2)}$-p. In other words, it is an antibonding state between $O_{(2)} - p$ in the CoO_2 layer and Co-d-$x^2 - y^2$ orbital with mostly O character. The corresponding bonding states with the highest majority spin Co $x^2 - y^2$ character lie near -6 eV, indicating that the majority spin Co states of this orbital lie indeed below the O-p states with which they form σ bonds. The conduction band minimum, which nominally occurs at M but corresponds to a rather flat band, has predominantly minority spin $3z^2 - r^2$ character on Co and a much smaller O-p character. In other words, the antibonding states of minority spin have Co character. We can further see that the very bottom of
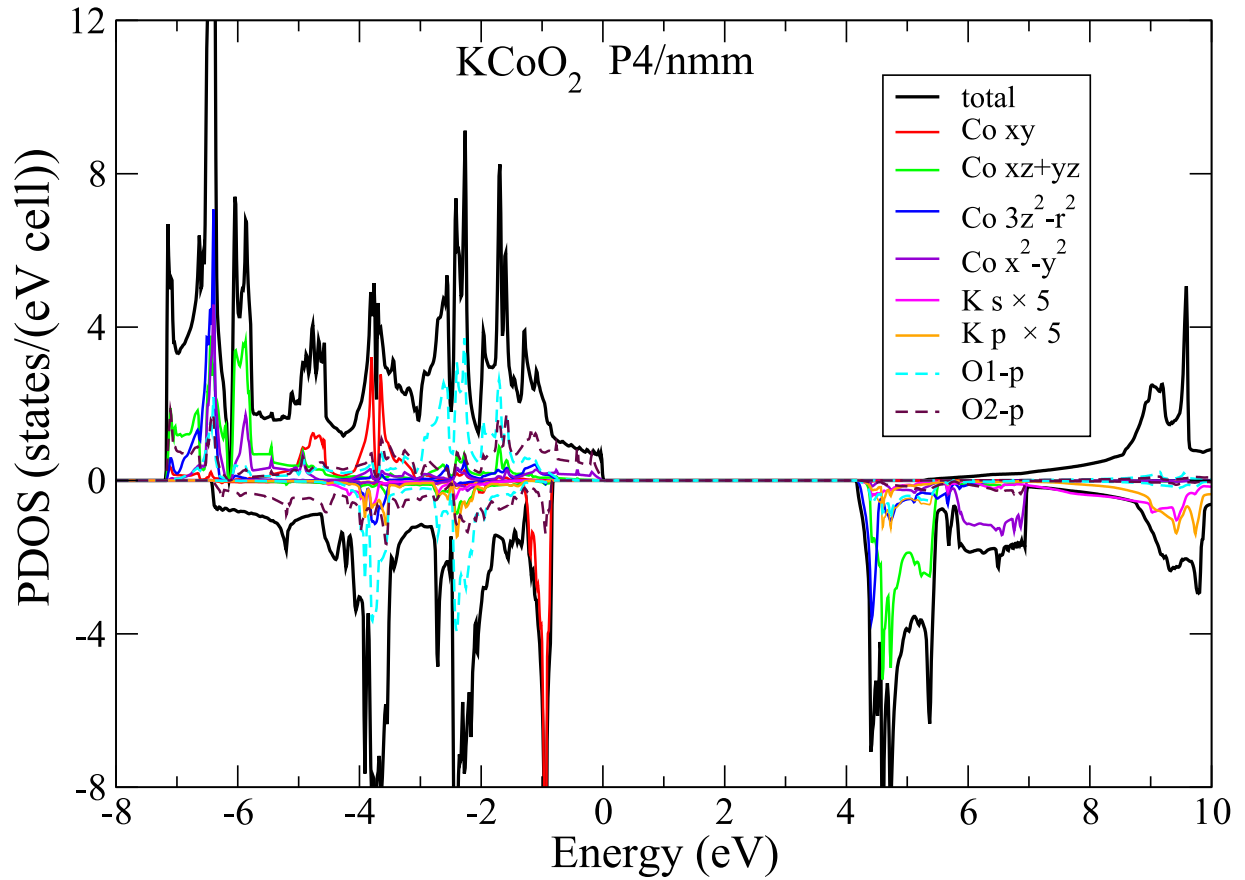
FIG. 4. Total and partial densities of states for $KCoO_2$ in $P4/nmm$ structure.

the valence bands have strong xz, yz majority spin character, while their minority spin counterparts are centered about 1 eV above the CBM. The xy derived bands have a notably smaller spin splitting. One can detect some xy character indicated in green in Fig. 5 (bottom panels) for both spins over a wide energy range in the valence band, from the very bottom to about -1 eV for minority spin and -3 eV for majority spin. This is an indication of their stronger dispersion, which we relate to direct Co-Co hopping along the [110] direction. This delocalization of xy-like states is responsible for its lower exchange splitting, which ultimately results in xy-like states being occupied for both spins.

Because of the dominant O character of the VBM and the Co character of the CBM, direct optical transitions from the VBM to the CBM can be characterized as charge transfer type, but would only be allowed for circularly polarized light because they are from spin-up to spin-down. For linearly polarized light, the optical transitions would be mostly between the minority spin bands, which are both quite flat and have both Co-d character, however, with xy character for the VBM of minority spin and $3z^2 - r^2$ character for the conduction band minimum. This would require a change of m orbital character of $\Delta m = 2$ and is therefore forbidden in the electric dipole approximation. Such rules, of course, only strictly apply in spherical symmetry and the symmetry breaking of the crystal can make them allowed but one might still expect rather weak transitions. On the other hand, for majority spin, the transitions would be indirect and therefore also forbidden.

These optical properties are rather unique and intriguing. The optical properties are further discussed in Sec. III D.

B. Magnetic ordering

Having established the formation of large magnetic moments as a basic way to stabilize the d^6 configuration in the unusual pyramidal environment, we now turn to the question of their ordering.

We start from the ferromagnetic unit cell with two Co atoms labeled 1 and 2, (note that in Fig. 8 these correspond to dark blue and grey squares) and use the procedure outlined in Sec. II. Table II shows some of the near-neighbor-exchange interactions and their cumulative sums. The J_{ab}^0 matrix has the form

$$J^0 = \begin{pmatrix} J_{11}^0 & J_{12}^0 \\ J_{12}^0 & J_{11}^0 \end{pmatrix} \qquad (7)$$

with eigenvalues $J_{11}^0 \pm J_{12}^0$, hence we find a mean-field $T_c = (2/3k_B)(J_{11}^0 - J_{12}^0)$ of -149 K. The negative value indicates that the system actually wants to order antiferromagnetically. Indeed, we find that the average spins on site 1 and 2 are opposite for the eigenvalue $J_{11}^0 - J_{12}^0$. However, we also see that the atoms in (100) neighboring cells also have a negative exchange interaction, which is in fact an order of magnitude larger. Thus, the system would prefer AFM ordering along the [110] direction, with parallel spins in (110) planes and
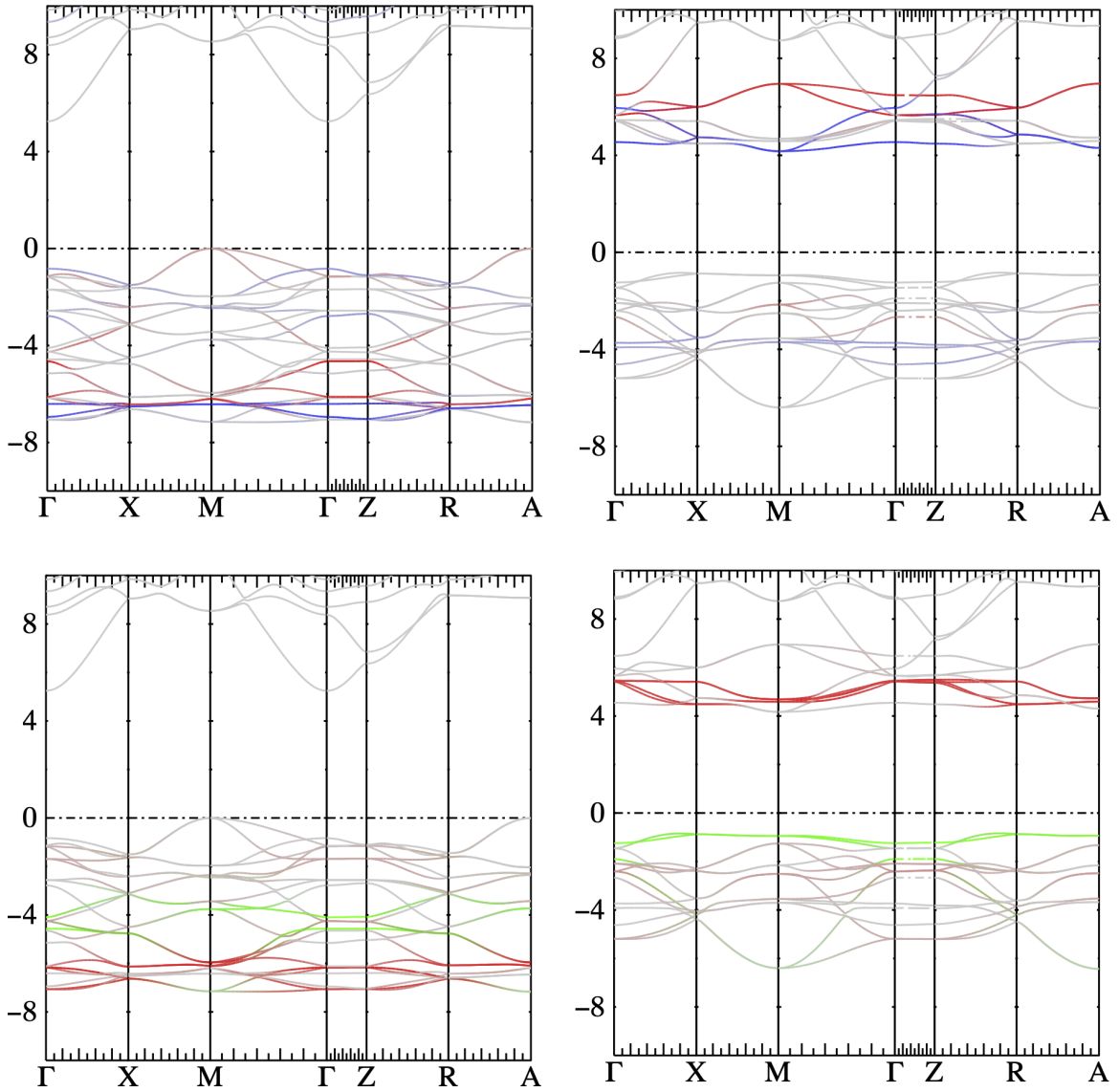
FIG. 5. Orbital weights of Co d of the bands, left for majority and right for minority spin; top row (red) $x^2 - y^2$ and (blue) $3z^2 - r^2$; bottom row (red) xz, yz and (green) xy.
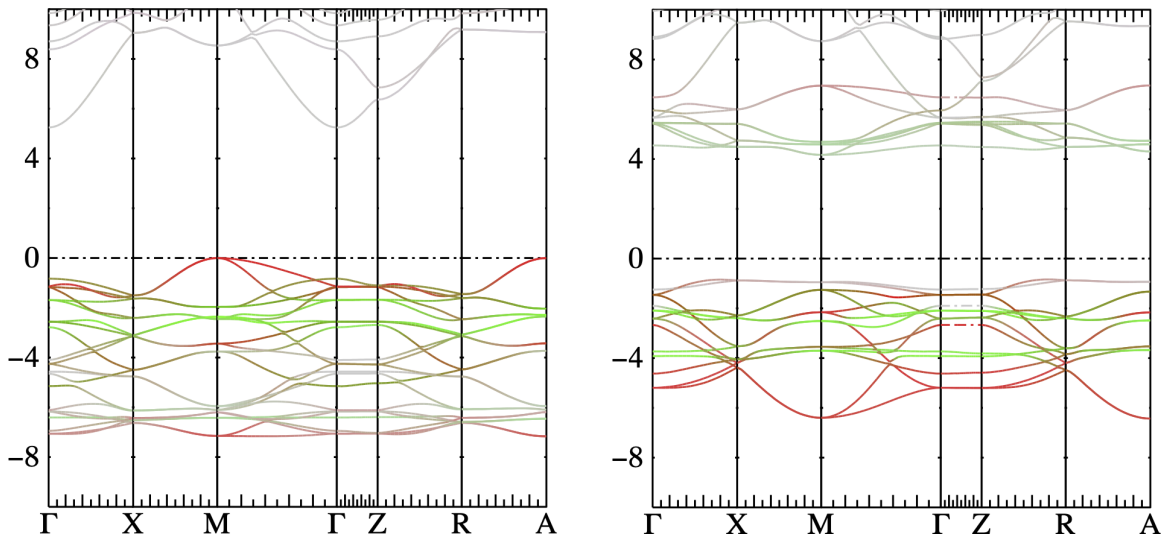

FIG. 6. Orbital weights of O p of the bands for left (majority) and right minority spin; red(O_2), green (O_1).
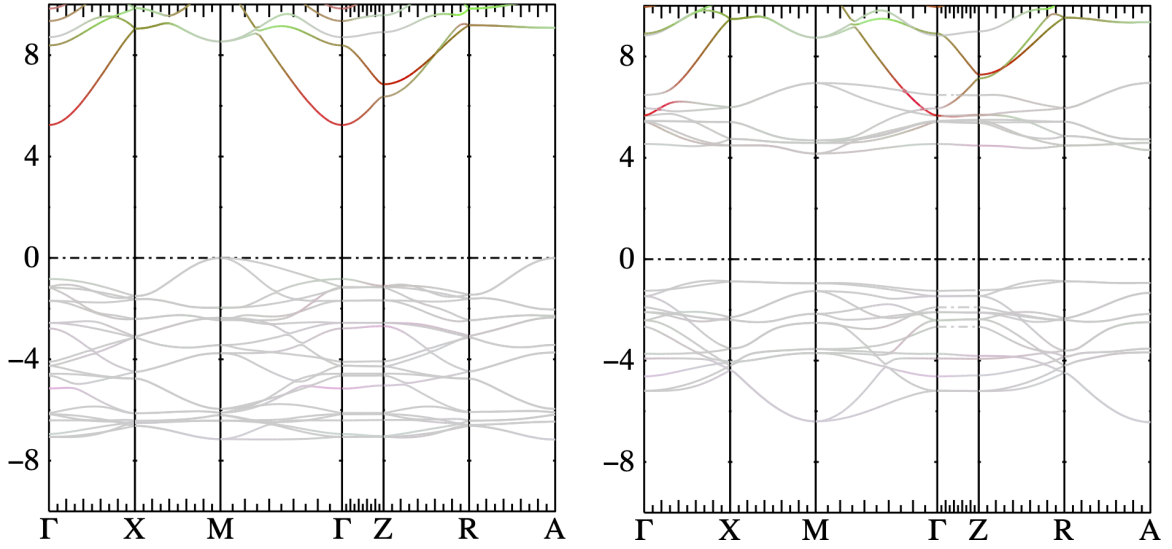
FIG. 7. Orbital weights of K s (red) and p (green) for left (majority) and right (minority) spin.

alternating up and down spin from plane to plane but also have the two atoms inside the cell with opposite spin.

The spin arrangement is illustrated in Fig. 8. Within the RPA method, we obtain a slightly lower critical temperature of 131 K. Given that the dominant exchange interaction corresponds to two Co atoms in line with an O in between, we can interpret this as an antiferromagnetic superexchange interaction, which might be dominated by the Co-d $x^2 - y^2$ σ bonds with O-p orbitals along the line. We can also see that the exchange interactions rapidly decrease beyond the first few neighbors.

Based on the above prediction of antiferromagnetic ordering, we then construct a doubled cell rotated by 45° and
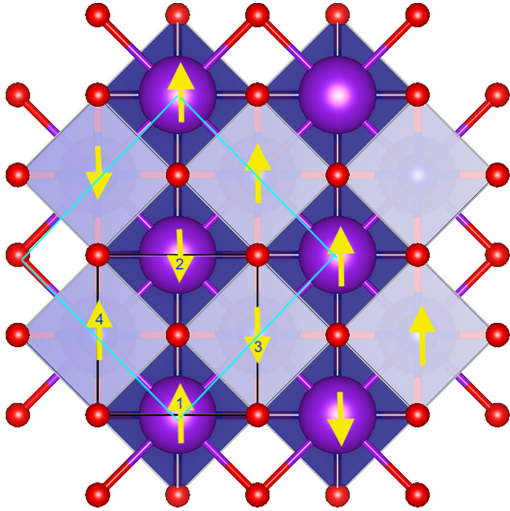

FIG. 8. Spin arrangement on the Co sites, the dark blue squares indicate the Co pyramid of Co slightly below the plane and the grey ones the Co slightly above the plane. The purple spheres are the K on top of the Co. The red spheres are the O and the yellow arrows indicate the spins on Co. The spins are labeled 1–4 in relation to Table III and Fig. 9 and the AFM unit cell is indicated by the light-blue line.

recalculate the exchange interactions based on this AFM reference state. We calculated the total energies in the GGA while adding the energy-independent self-energy matrix to the one-particle Hamiltonian to have the correct gaps. This gives $E_{AFM} - E_{FM} = -0.240\,\text{eV/Co atom}$. So, the AFM ordering is definitely preferable. Setting $E_{AFM} - E_{FM} = 2zJ_{\text{eff}}$ with $z = 4$ the number of neighbors, this corresponds to an effective AFM exchange interaction $J_{\text{eff}} = -30\,\text{meV}$. In the mean-field approximation $T_N = 2J_{\text{eff}}/3k_B$ and we find $T_N \approx 232\,\text{K}$. However, this assumes there is only an effective nearest-neighbor interaction.

Next, we calculate again the exchange interactions from the magnetic susceptibility for this case. We now have four magnetic sites per cell as labeled in Fig. 8. The exchange interactions between near neighbors are given in Table III and plotted as a function of distance in Fig. 9.

One can note that the cumulative sum only slowly converges. The nearest-neighbor interactions between atoms 1 and 2 in the AFM cell corresponds to the interaction between

TABLE II. Exchange interactions in mRy; a and b label the magnetic atoms in the cell, $\mathbf{T}$ gives the lattice vector in reduced coordinates, z the number of equivalent neighbors in the star, $J_{ab}^{0\mathbf{T}}$ the exchange interaction in mRy, and the last column gives the cumulative sum, with the last row for a given block of a, b giving the cumulative sum up to $|\boldsymbol{\tau}_a - \boldsymbol{\tau}_b - \mathbf{T}| < r_{cut} = 5$ in units of the in-plane tetragonal lattice constant a.

a	b	$\mathbf{T}$	z	$J_{ab}^{0\mathbf{T}}$	$\sum_{\mathbf{T}} J_{ab}^{0\mathbf{T}}$
1	1	(1,0,0)	4	−0.3725	−1.490
1	1	(1,1,0)	4	−0.0362	−1.635
1	1	(2,0,0)	4	0.0012	−1.630
1	1	…			−1.561
1	2	(0,0,0)	4	−0.0342	−0.137
1	2	(1,0,0)	8	0.0024	−0.118
1	2	(0,0,1)	4	−0.0024	−0.127
1	2	…			−0.137

TABLE III. Exchange interactions in [110] AFM cell; magnetic atom labels a, b, lattice vector (in Cartesian coordinates and units of a in x, y directions and c in z direction) of the $P4/nmm$ primitive cell, number of equivalent atoms in the star, J_{ab}^{0T} in mRy and their cumulative sum.

| a	b	T	z	J_{ab}^{0T}	$\sum_T J_{ab}^{0T}$
1	1	$(-1, 1, 0)$	2	0.0525	0.105
1	1	$(1,1,0)$	2	−0.0174	0.070
1	1	$(0,2,0)$	4	−0.0518	−0.137
1	1	$(0, 0, \pm1)$	2	−0.0002	−0.138
1	1	$(-1, 1, \pm1)$	4	0.0035	−0.124
1	1	$(1, 1, \pm1)$	4	−0.0003	−0.125
1	1	$(2,2,0)$	2	0.016	−0.093
1	1	$(-2, 2, 0)$	2	−0.0107	−0.111
1	1	$(2, 0, \pm1)$	8	0.0009	−0.107
1	2	$(1,0,0)$	4	−0.6139	−2.456
1	2	$(1,2,0)$	4	−0.0019	−2.463
1	2	$(-2, 1, 0)$	4	−0.0006	−2.466
1	2	$(1,0,1)$	8	−0.0002	−2.467
1	2	$(0,3,0)$	4	0.0006	−2.465
1	2	$\dots$			−2.464
1	3	$(0,0,0)$	2	−0.1144	−0.229
1	3	$(0,1,0)$	4	0.0020	−0.221
1	3	$(0, 0, -1)$	2	−0.0016	−0.224
1	3	$(1,1,0)$	2	−0.0012	−0.226
1	3	$(0.1, -1)$	4	−0.0010	−0.227
1	3	$\dots$			−0.231
1	4	$(0,0,0)$	2	−0.1538	−0.308
1	4	$(0,1,0)$	4	−0.0263	−0.413
1	4	$(0, 0, -1)$	2	0.0080	−0.397
1	4	$(-1, 1, 0)$	2	0.0518	−0.293
1	4	$(0, 1, -1)$	4	−0.0003	−0.294
1	4	$(0,0,1)$	2	0.0009	−0.292
1	4	$(0,2,0)$	4	0.0162	−0.228
1	4	$(-1, -1, -1)$	2	0.0044	−0.219
1	4	$(0,1,1)$	4	0.0008	−0.216
1	4	$(2,1,0)$	4	0.0106	−0.173
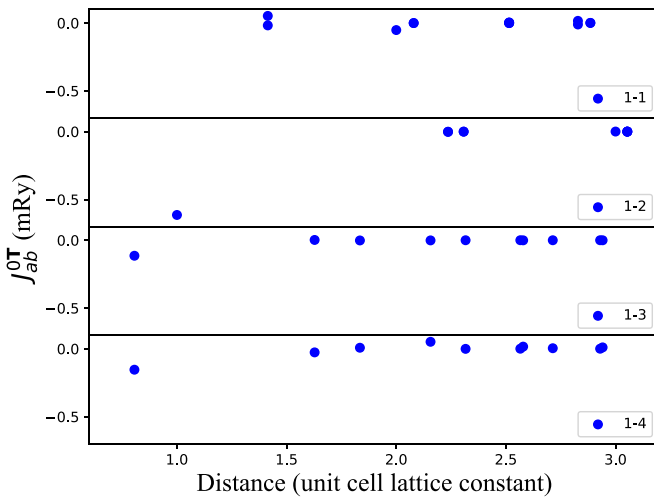
FIG. 9. Exchange interactions in AFM case as function of distance. The labels in each panel correspond to the atom pairs ab in the AFM unit cell as identified in Fig. 8. The distance on the horizontal axis is $|\boldsymbol{\tau}_a - \boldsymbol{\tau}_b - \mathbf{T}|$.

atoms 1 in neighboring cells in the (100) direction in the FM cell and is seen to be the dominant interaction, which is antiferromagnetic. Its value −0.6139 is almost twice as large as when we started from the FM reference state, −0.3725. The nearest interactions between 1 and 3 correspond to the interaction between the Co originally in the same FM cell and between Co slightly above and slightly below the plane. Its value is −0.1144, which is also about three times larger in absolute value than in the FM cell. Similarly, the interaction between 1 and 4, which also corresponds to 1 and 2 in the FM cell is even larger at −0.1538. All of these values are in mRy. The matrix of exchange interactions in this case has the form

$$J^0 = \begin{pmatrix} a & b & c & d \\ b & a & d & c \\ c & d & a & b \\ d & c & b & a \end{pmatrix} \tag{8}$$

with $a = -0.107$, $b = -2.464$, $c = -0.231$, and $d = -0.173$. Its largest eigenvalue is $a - b - c + d$ and yields a mean-field temperature of 254 K. The Tyablikov approach yields a significant reduction to 97 K. The spin arrangement of atoms 1,2,3,4 is ↑↓↓↑, which in fact, the same as the reference state we started from, so that now the T_c indeed comes out positive. Also, note that the mean-field estimate here is close to the very simple model with an effective J_{eff} obtained from the AFM-FM total energy difference. That effective interaction represents the sum over all individual exchange interactions in the periodic system, in other words the $J_{12}^0 = \sum_T J_{12}^{0T}$, excluding the on-site term, which indeed is −2.464 mRy corresponding to 259 K. So, these different ways of estimating the mean-field T_c are roughly consistent with each other. Comparing with the prediction starting from the FM reference state, we consistently obtain an AFM ordering along alternating (110) planes and all spins in these planes parallel, both in the down-pointing and up-pointing square Co pyramids, or the two sites in the primitive cell. The mean-field approach gives a substantially larger T_c when starting from the AFM reference state, but the final RPA estimates, which are expected to give a lower bound are not that far from each other 93 K vs 130 K. Thus, we can safely conclude that the Néel temperature is approximately 100 K.

The large value of the exchange interaction between Co in line with the O between nearest-neighbor primitive cells suggests that it is derived from superexchange via the O between $d_{x^2-y^2}$ orbitals. The AFM interaction between the two Co within the primitive cell on the other hand, is likely to be a direct interaction between d_{xy} orbitals, which would nearly point to each other except that the Co atoms are in slightly different horizontal planes. The d_{xz}, d_{yz} orbitals or their superposition along a [110] direction could also contribute to this via direct antiferromagnetic coupling.

The magnetic ordering is thus rather interesting with large magnetic moments of 4 μ_B interacting differently via the different Co-d orbitals involved. The dominant interaction is superexchange but a smaller direct interaction between atoms in the same unit cell also plays a role. One might speculate that spin fluctuations of this smaller interactions combined with doping to create a metallic state, either p or n-type doping might lead to interesting effects and possibly
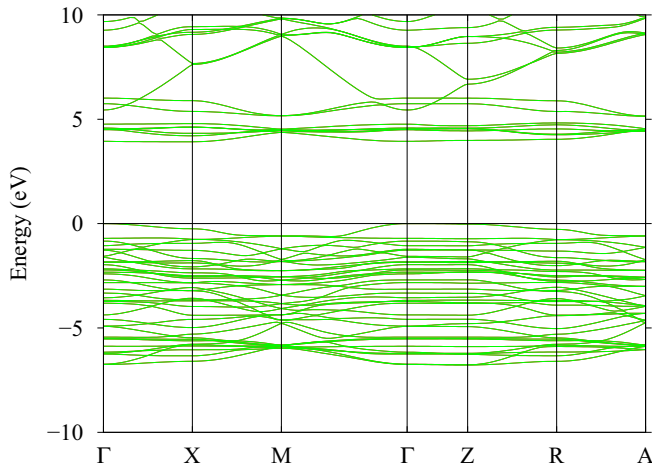
FIG. 10. Band structure of AFM KCoO$_2$ in the QSGW approach.

spin fluctuations mediated superconductivity. We hasten to say that at this moment this is a speculative point. However, an antiferromagnetic parent compound with Mott-insulating behavior as we find here, since the occurrence of the gap is related to the magnetic moment stabilization, is the generic scenario from which doping and spin fluctuations can lead to superconductivity. A study of the doping and its consequences is beyond the scope of the present study as it might require more advanced methods to treat strong correlations in the rather flat band edges.

C. AFM band structure

The antiferromagnetic band structure is shown in Fig. 10. The relation between the FM primitive cell Brillouin zone and the AFM cell Brillouin zone is shown in Fig. 11. The new $\Gamma - X$ direction is half the old $\Gamma - M$ direction and the bands are essentially folded in two in that direction. The new M point corresponds to the old X point. The band structure now has a direct gap at Γ of 3.94 eV because the spin up VBM state at M becomes folded on the new Γ state. Both the top valence and bottom conduction bands become almost entirely flat along ΓZ.
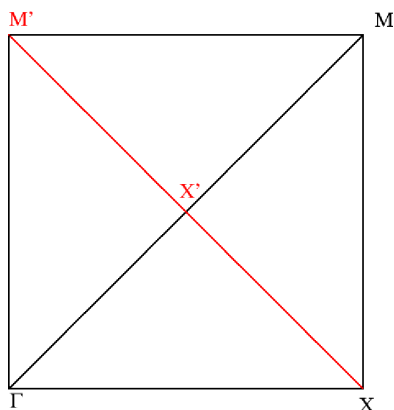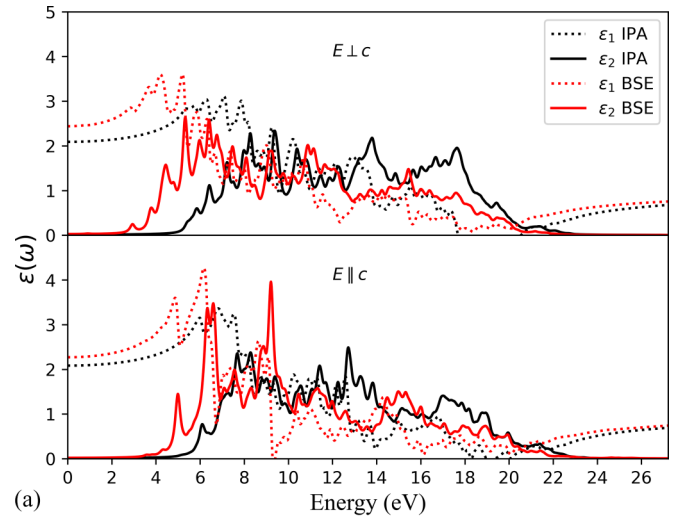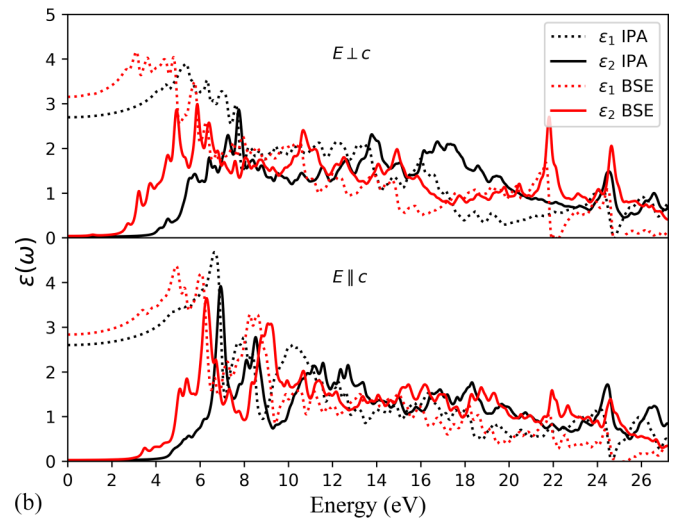

FIG. 11. Relation between primitive cell tetragonal Brillouin zone labeled in black and doubled cell 45 degree rotated Brillouin zone for AFM case, labeled in red and with primes.

FIG. 12. Optical dielectric function for two polarizations in IPA and BSE, assuming transitions only between the equal spins for (a) FM and (b) AFM case.

D. Optical dielectric function

The optical dielectric function was calculated assuming only transitions between majority to majority spin states, and minority to minority spins, treated separately. They were calculated in the independent-particle approximation (IPA) and using the Bethe-Salpeter equation (BSE), which includes local field and electron-hole interaction effects. The results are shown for both the real and imaginary part in Fig. 12. Within both IPA and BSE, we assume here that the allowed dipole transitions are spin separated. Strictly speaking, the exchange Coulomb interaction matrix elements in the BSE

$$V_{vc\mathbf{k}v'c'\mathbf{k}'} = \int d(1)d(2)\psi_{v\mathbf{k}}(1)\psi_{c\mathbf{k}}(1)^* v(|\mathbf{r} - \mathbf{r}'|)$$
$$\times \psi_{v'\mathbf{k}'}(2)^* \psi_{c'\mathbf{k}'}(2) \tag{9}$$

require the valence (v) and conduction (c) band at one $\mathbf{k}$ to have the same spin and also at the other $\mathbf{k}'$ point because the integral over coordinates (1) or (2) includes spin summation, but the spins of $vc\mathbf{k}$ and $v'c'\mathbf{k}'$ may differ. So, an interaction between up and down spin band-to-band transitions
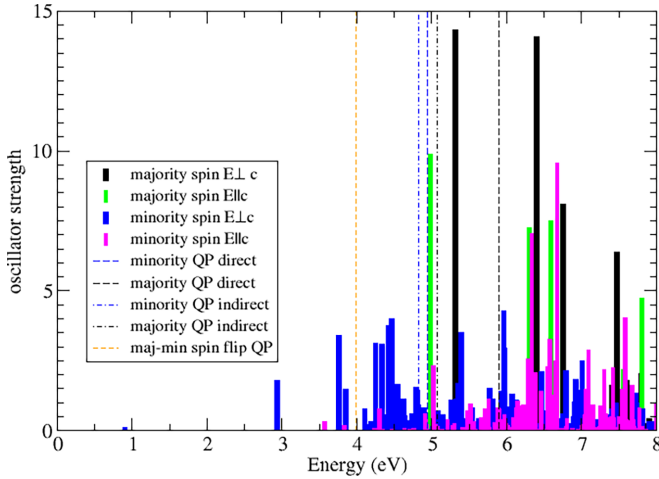
FIG. 13. Oscillator strengths of two-particle levels and quasiparticle gaps.

is mediated by the exciton exchange interaction $V_{vc\mathbf{k},v'c'\mathbf{k'}}$. However, if the optical transitions of the separated spins are sufficiently well separated, we may ignore this interaction. This is the approximation we currently are making. Note that for nonspin-polarized systems, this is manifestly not the case since the up-up and down-down transitions are degenerate. However, in that case the spin structure of the excitons is clear [23] and leads to dark spin triplets involving only the $-W$ matrix elements with the screened Coulomb interaction, whereas the spin-singlet ones involve $2\bar{V} - W$ with $\bar{V}$ the microscopic part of the above defined exciton exchange interactions (i.e., excluding the average or long-range macroscopic interaction). At present we include $\bar{V} - W$ but separately for each spin. In the calculation in Fig. 12 we include 24 valence bands and 16 conduction bands for the FM case. This includes the 12 O-2p bands and 10 Co-d bands of each spin. For the AFM case, the spin-up and spin-down levels are again degenerate but the eigenstates forming the basis of the two-particle Hamiltonian to be diagonalized in BSE are not the same since the spin-up and spin-down contributions are on different atoms in the cell. Thus, one may expect that the Coulomb matrix elements between $vc\mathbf{k}$ of spin-down and spin-down are small. In that sense it is again reasonable to neglect them.

With this understanding of the approximations made, we now examine the results. First, we may note that the electron-hole effects have a significant impact with excitonic peaks occurring below the quasiparticle gap. Interestingly, there seems to be almost a uniform red shift of $\sim$2 eV from IPA to BSE. The sharp peaks below the lowest direct quasiparticle gap between equal spins, of about 5.0 eV according to Table I, indicates excitonic transitions. Excitons with large binding energies were recently also found to occur in other layered oxides, such as LiCoO$_2$ [24,25] and V$_2$O$_5$ [26,27]. Figure 13 shows the two-particle Hamiltonian eigenvalues with their oscillator strengths separately for majority and minority spin transitions. We can see that the lowest peaks in the $\varepsilon_2(\omega)$ correspond to transitions between minority spin bands. We also indicate the lowest indirect and direct quasiparticle gaps for both majority and minority spin bands and the forbidden spin-flip quasiparticle gap. Clearly, the peaks below about

5 eV are all excitonic in nature. We can also discern an almost dark exciton just below 1 eV. A detailed study of the nature of these excitons is postponed to future work. We note, however, that they appear to be primarily transitions between Co minority spin states for the FM case.

Next, we caution that the optical matrix elements of the velocity matrix elements may be overestimated because of difficulties in evaluating the contributions from the nonlocal self-energy operator of the GW approximation, which require estimating the $d\Sigma/dk$ numerically. This has been found in other systems to overestimate the magnitude of $\varepsilon_2(\omega)$ compared to evaluating the $\varepsilon_2(\mathbf{q}, \omega)$ at finite small $\mathbf{q}$ and then extrapolating to $\mathbf{q} \rightarrow 0$ numerically. This then also leads to an overestimate of the $\varepsilon_1(\omega)$ below the gap and in particular its limit $\lim_{\omega \to 0} \varepsilon_1(\omega)$, which gives the electronic screening at the static limit. This "static limit" does not include phonon contributions (conventionally referred to as ε_∞) and corresponds to the square of the index of refraction n^2 in the range sufficiently well below the gap, but higher than any of the phonon modes. Also, at present we cannot yet calculate the transitions between up and down spin bands, which would be of great interest in this system, but are expected to occur only for circularly polarized light.

The optical dielectric function of the AFM state is shown in Fig. 12(b). It is calculated here using $N_v = 48$ valence bands and $N_c = 40$ conduction bands and a $3 \times 3 \times 3$ **k** mesh. It is rather similar to the corresponding FM case shown in Fig. 12 although not quite identical. In both cases, we may note a substantial redshift between the IPA and BSE $\varepsilon_2(\omega)$ and excitonic features below the quasiparticle gap of 3.94 eV. The lowest excitons with quite small oscillator strength occur near 1 eV. We note that the sharp features for **E** $\perp$ **c** at 22 and 24 eV may be artifacts of the truncation of the active space in the BSE calculation. For a smaller set, similar features appeared for **E** $\parallel$ **c** around 15 eV but these disappear or are weakened when more conduction bands were included. The calculation may be deemed to be converged up to about 12 eV as in this range they are the same with higher or lower N_c.

IV. CONCLUSIONS

The main conclusions from our study are summarized as follows. KCoO$_2$ has large magnetic moments of $4\mu_B$ on the Co atoms, corresponding to a d_{xy}^2, $\{d_{xz}, d_{yz}\}_\uparrow^2$, $\{d_{x^2-y^2}\}_\uparrow^1$, $\{d_{3z^2-r^2}\}_\uparrow^1$ configuration, arising from the square pyramidal coordination with a K ion on the opposing apical site. The magnetic moments prefer to order antiferromagnetically along the [110] direction. The exchange interactions are dominated by an antiferromagnetic super-exchange coupling between $d_{x^2-y^2}$ orbitals σ bonding with O-p orbitals between them in a 180° alignment of order $\sim$8 meV but with smaller direct exchange between the two Co per primitive cell, thus aligning all spin on atoms in successive (110) planes. The Néel temperature was predicted to be about 100 K using the Tyablikov-Callen approach and using exchange interactions extracted from the transverse spin susceptibility in a rigid-spin approximation per sphere and including a converged summation of exchange interactions. In the mean-field approximation, a larger critical temperature of about 250 K is

obtained, which provides an upper limit. In the ferromagnetic state, the band structure exhibits an indirect gap between the conduction band minimum at Γ of minority spin and a valence band maximum of majority spin at M, the corner of the Brillouin zone in the $k_z = 0$ plane. The optical transitions between equal spin were calculated including electron-hole interaction effects and show strongly bound excitons arising primarily from minority spin electron-hole pairs. In the AFM case, the band edges of the gap show extremely flat regions along the direction perpendicular to the layers and a direct quasiparticle gap of 3.94 eV. The combination of large magnetic moments, relatively small exchange interactions of different types and flat band edge states indicate that strong correlation effects may be present in this system and could lead to interesting effects, in particular when doping is considered to modify the antiferromagnetic insulating ground state.

[1] M. Jansen and R. Hoppe, Zur Kenntnis von $KCoO_2$ und $RbCoO_2$, Z. Anorg. Allg. Chem. **417**, 31 (1975).

[2] C. Delmas, C. Fouassier, and P. Hagenmuller, Les bronzes de cobalt K_xCoO_2 ($x < 1$). L'oxyde $KCoO_2$, J. Solid State Chem. **13**, 165 (1975).

[3] M. I. Frei, Synthesis and characterization of ternary transition-metal oxides featuring low-dimensional structural elements, Ph.D. thesis, Technische Universität Dresden, 2021.

[4] K. Li, X. Fan, D. J. Singh, and W. Zheng, Search for potential K ion battery cathodes by first principles, J. Energy Chem. **54**, 377 (2021).

[5] J. P. Perdew, K. Burke, and M. Ernzerhof, Generalized gradient approximation made simple, Phys. Rev. Lett. **77**, 3865 (1996).

[6] L. Hedin, New method for calculating the one-particle Green's function with application to the electron-gas problem, Phys. Rev. **139**, A796 (1965).

[7] L. Hedin and S. Lundqvist, Effects of electron-electron and electron-phonon interactions on the one-electron states of solids, in *Solid State Physics, Advanced in Research and Applications*, edited by F. Seitz, D. Turnbull, and H. Ehrenreich (Academic Press, New York, 1969), Vol. 23, pp. 1–181.

[8] T. Kotani, M. van Schilfgaarde, and S. V. Faleev, Quasiparticle self-consistent GW method: A basis for the independent-particle approximation, Phys. Rev. B **76**, 165106 (2007).

[9] M. van Schilfgaarde, T. Kotani, and S. Faleev, Quasiparticle self-consistent *GW* theory, Phys. Rev. Lett. **96**, 226402 (2006).

[10] D. Pashov, S. Acharya, W. R. Lambrecht, J. Jackson, K. D. Belashchenko, A. Chantis, F. Jamet, and M. van Schilfgaarde, Questaal: A package of electronic structure methods based on the linear muffin-tin orbital technique, Comput. Phys. Commun. **249**, 107065 (2019).

[11] E. Bott, M. Methfessel, W. Krabs, and P. C. Schmidt, Nonsingular Hankel functions as a new basis for electronic structure calculations, J. Math. Phys. **39**, 3393 (1998).

[12] G. Onida, L. Reining, and A. Rubio, Electronic excitations: Density-functional versus many-body Green's-function approaches, Rev. Mod. Phys. **74**, 601 (2002).

[13] B. Cunningham, M. Grüning, D. Pashov, and M. van Schilfgaarde, $QSG\hat{W}$: Quasiparticle self-consistent *GW* with ladder diagrams in W, Phys. Rev. B **108**, 165104 (2023).

[14] T. Kotani and M. van Schilfgaarde, Spin wave dispersion based on the quasiparticle self-consistent GW method: NiO, MnO and α-MnAs, J. Phys.: Condens. Matter **20**, 295214 (2008).

[15] V. Antropov, The exchange coupling and spin waves in metallic magnets: Removal of the long-wave approximation, J. Magn. Magn. Mater. **262**, L192 (2003).

[16] A. Liechtenstein, M. Katsnelson, V. Antropov, and V. Gubanov, Local spin density functional approach to the theory of exchange interactions in ferromagnetic metals and alloys, J. Magn. Magn. Mater. **67**, 65 (1987).

[17] S. V. Tyablikov, Retarded and advanced Green functions in the theory of ferromagnetism, Ukr. Mat. Zh. **11**, 287 (1959).

[18] H. B. Callen, Green function theory of ferromagnetism, Phys. Rev. **130**, 890 (1963).

[19] J. Rusz, I. Turek, and M. Diviš, Random-phase approximation for critical temperatures of collinear magnets with multiple sublattices: GdX compounds (X = Mg, Rh, Ni, Pd), Phys. Rev. B **71**, 174408 (2005).

[20] E. Şaşıoğlu, L. M. Sandratskii, and P. Bruno, First-principles calculation of the intersublattice exchange interactions and Curie temperatures of the full Heusler alloys Ni_2MnX (X = Ga, In, Sn, Sb), Phys. Rev. B **70**, 024427 (2004).

[21] Data retrieved from Materials Project for $KCoO_2$ (mp-20528).

[22] A. Jain, S. P. Ong, G. Hautier, W. Chen, W. D. Richards, S. Dacek, S. Cholia, D. Gunter, D. Skinner, G. Ceder, and K. A. Persson, Commentary: The Materials Project: A materials genome approach to accelerating materials innovation, APL Mater. **1**, 011002 (2013).

[23] M. Rohlfing and S. G. Louie, Electron-hole excitations and optical spectra from first principles, Phys. Rev. B **62**, 4927 (2000).

[24] S. K. Radha, W. R. L. Lambrecht, B. Cunningham, M. Grüning, D. Pashov, and M. van Schilfgaarde, Optical response and band structure of $LiCoO_2$ including electron-hole interaction effects, Phys. Rev. B **104**, 115120 (2021).

[25] S. K. Radha, W. R. L. Lambrecht, B. Cunningham, M. Grüning, D. Pashov, and M. van Schilfgaarde, Erratum: Optical response and band structure of $LiCoO_2$ including electron-hole interac-

tion effects [Phys. Rev. B **104**, 115120 (2021)], Phys. Rev. B **108**, 159902(E) (2023).

[26] V. Gorelov, L. Reining, M. Feneberg, R. Goldhahn, A. Schleife, W. R. L. Lambrecht, and M. Gatti, Delocalization of dark and bright excitons in flat-band materials and

the optical properties of V_2O_5, npj Comput. Mater. **8**, 94 (2022).

[27] C. Garcia, S. K. Radha, S. Acharya, and W. R. L. Lambrecht, Quasiparticle band structure and excitonic optical response in V_2O_5 bulk and monolayer, arXiv:2403.05473.